Journal of Archaeological Science: Reports 39 (2021) 103162

Contents lists available at ScienceDirect

Journal of Archaeological Science: Reports

journal homepage: www.elsevier.com/locate/jasrep

# What causes differences in fracture rates of silcrete during heat treatment? A near-infrared study of water-related transformations in South African silcretes

Sara Watson [a,*], Shezani Nasoordeen [b], Mark N. Grote [a], Alex Mackay [b], Patrick Schmidt [c,d]

[a] *Department of Anthropology, University of California, Davis, CA 95616, USA*
[b] *Centre for Archaeological Science, School of Earth, Atmospheric, and Life Sciences, University of Wollongong, Wollongong, NSW 2522, Australia*
[c] *Department of Prehistory and Quaternary Archaeology, Eberhard Karls University of Tübingen, 72070 Tübingen, Germany*
[d] *Department of Geosciences, Applied Mineralogy, Eberhard Karls University of Tübingen, 72074 Tübingen, Germany*

ARTICLE INFO

*Keywords:*
Heat treatment
Silcrete
South Africa
Middle stone age
Lithic technology
Silica rocks
Near FTIR

ABSTRACT

Discussions of heat treatment in the southern African Middle Stone Age often focus on the importance of this innovation to the development of complex technologies and the evolution of modern human cognition. Debates regarding the context of silcrete heat treatment typically include the amount of time and resource investment needed, and when the earliest occurrences of heat treatment appear in the archaeological record. However, silcrete is a heterogeneous material and the potential effects of this heterogeneity on the thermal transformations that occur during heat treatment are not well established. We undertook a series of controlled experiments using direct transmission near-infrared spectroscopy on South African silcretes from multiple sources heated to a range of maximum temperatures to examine the degree of heterogeneity in starting structural content and the evolution of thermal transformations. We found that material source is an important determinant of starting concentrations of $H_2O$, SiOH, and pore space in silcrete, as well as the thermal evolution of these variables. These results shed light on the degree and sources of variation in the structural content and thermal behavior of silcrete during heat treatment and allow for a better understanding of the heterogeneity of silcrete as a raw material and the implications of this for African Middle Stone Age pyrotechnology.

## 1. Introduction

Heat treatment, the intentional alteration of lithic raw materials to improve their quality for tool production, is viewed as an important technological innovation in human evolution. The use of heat treatment has been documented in contexts across the globe during the late Pleistocene and Holocene, but the earliest known occurrence is found during the Middle Stone Age (MSA) of southern Africa (Brown et al., 2009; Schmidt et al., 2020). With its rich archaeological record, southern Africa has been important to our understanding of the behavioral evolution of our species. During the MSA we see an expansion of the material culture record and technological repertoire of early modern humans to include the use of pressure flaking (Mourre et al., 2010), bone tool production (Henshilwood et al., 2001; Backwell et al., 2008), creation of hafting adhesives (Wadley, 2010), and the potential early use of projectiles (Pargeter, 2007; Lombard and Wadley, 2016) in addition to heat treatment of silcrete for tool making. Modes of controlled and uncontrolled heat treatment are not well understood in the context of this behavioral repertoire.

Silcrete is a silica rock, a classification which also includes quartzite, some of the sandstones, flint and chert. Silica rocks are all composed of quartz crystals, but their formation processes, grain size, and microstructure vary (Tucker, 2009). In metasomatic silica rocks like flint or chert (henceforth only called chert) and silcrete, 'water' forms part of the structure as molecular ($H_2O$) and chemically bound water (silanol, SiOH) (Graetsch et al., 1987; Kronenberg, 1994). During heat treatment, transformations within these rocks involve $H_2O$ and SiOH, as well as the rock's network of intergranular pores that may adsorb water (Micheelsen, 1966; Flörke et al., 1982; Graetsch et al., 1985; Fukuda et al., 2009; Roqué-Rosell et al., 2011; Schmidt et al., 2011; Schmidt et al., 2012). Hydrogen bonds (H-bonds) are formed with silanol along the crystalline structure of open pore walls. Bonds are also formed with molecular

---

[*] Corresponding author.
*E-mail address:* sewatson@ucdavis.edu (S. Watson).

https://doi.org/10.1016/j.jasrep.2021.103162
Received 27 October 2020; Received in revised form 5 August 2021; Accepted 15 August 2021

water held within pores (Graetsch et al., 1985; Schmidt et al., 2011; Schmidt et al., 2017a). Beginning around 200 °C, silanol at the surface of pore walls and perhaps also within other defect sites is 'converted' to water through the reaction Si–OH ··· OH–Si → Si–O–Si + $H_2O$ (Schmidt et al., 2011; Schmidt et al., 2017a), resulting in new Si–O–Si bonds between quartz crystals. $H_2O$ and SiOH are evacuated through the intergranular pores and the pores begin to close (Schmidt, 2014).

Testing of the mechanical properties of heat-treated silica rocks showed a reduction in fracture toughness as a result of the previously described chemical and crystallographic changes (Schindler et al., 1982; Domanski et al., 1994; Schmidt et al., 2018). These changes lead to better force transmission during fracture (as in tool knapping), leaving behind recognizably smoother fracture negatives than in the unheated rock (Schmidt et al., 2018), flake detachment requiring less force (Domanski et al., 1994; Schmidt et al., 2018), and the production of larger and longer flakes (Bleed and Meier, 1980; Pargeter and Schmidt, 2020). Differences in structural composition affect the heating tolerances of silica rocks, or the maximum temperatures and heating ramp rates that can be applied to a rock without fracture failure. If surface pores close before enough water has been evacuated, water accumulates in fluid inclusions. Buildup of pressure in these fluid inclusions is strong enough to induce fracturing of the rock (termed overheating, (Schmidt, 2014)).

In a recent paper, Mackay et al. (2018) examined the tolerance of silcretes from multiple sources in Australia and South Africa to high heating rates. Controlling for sample volume and heating rate, they found significant variation in probability of sample failure between sources, to the extent that silcretes from some sources always fractured at high heating rates while silcretes from other sources almost never fractured under the same conditions. While offering conjectures as to the implications of these observations for the past practice of heat treatment, they did not explore the causes underlying observed variation.

For the present paper, we undertook a series of controlled laboratory experiments using near-infrared (NIR) spectroscopy to examine thermal changes in $H_2O$, SiOH, and pore space to understand the range of variability in silcretes from different sources in terms of their physical and chemical behavior during heating. We consider the effects of structural differences between rocks from different sources and observed differences in their response to heating with several questions in mind:

1. How much does structural composition change and what is the nature of this change?
2. What is the range of variation in silcrete behavior during heating?
3. What is the primary source of variance influencing silcrete thermal behavior?

## 2. Materials and methods

We analyzed nine samples from five sources (Fig. 1). Three derive from the Cederberg mountain region of South Africa, two of which are in the Doring River catchment (sources AGF, SWV) (n = 4) and the third from the Olifants River catchment (RG, n = 2). A further two sources derive from southern Namaqualand (MHS and ALF) (n = 3), the latter of which (ALF) is also situated in the Oilfants River catchment. All sources occur in primary contexts, though taking different forms; the Olifants River sources (ALF & RG) occur as large rafts in ancient river terraces, while AGF, MSH, and SWV occur as cobble mantles on ridge tops. Photos were taken using a macro lens with 4x magnification (Fig. 2) and texture descriptions of these samples following Summerfield (1983) can be found in Table 2.

MSH and ALF are visually consistent with artefacts recovered from the site Varsche Rivier 003 (Steele et al., 2016), and the land surface immediately above the outcrop at ALF (Fig. 1, top right panel) is covered in

**Fig. 1.** Location of silcrete sources sampled for this paper (yellow stars) along with major nearby archaeological sites (white triangles). Sources: AGF = Agtersfontein, ALF = Alfalfa, MSH = Mustard Source Hill, RG = Rondegat, SWV = Swartvlei. Archaeological sites: DRS = Diepkloof Rock Shelter, EBC = Elands Bay Cave, KFR = Klipfonteinrand, KKH = Klein Kliphuis, VR003 = Varsche Rivier 003. Base image is from ESRI ArcGIS online world imagery. (For interpretation of the references to colour in this figure legend, the reader is referred to the web version of this article.)

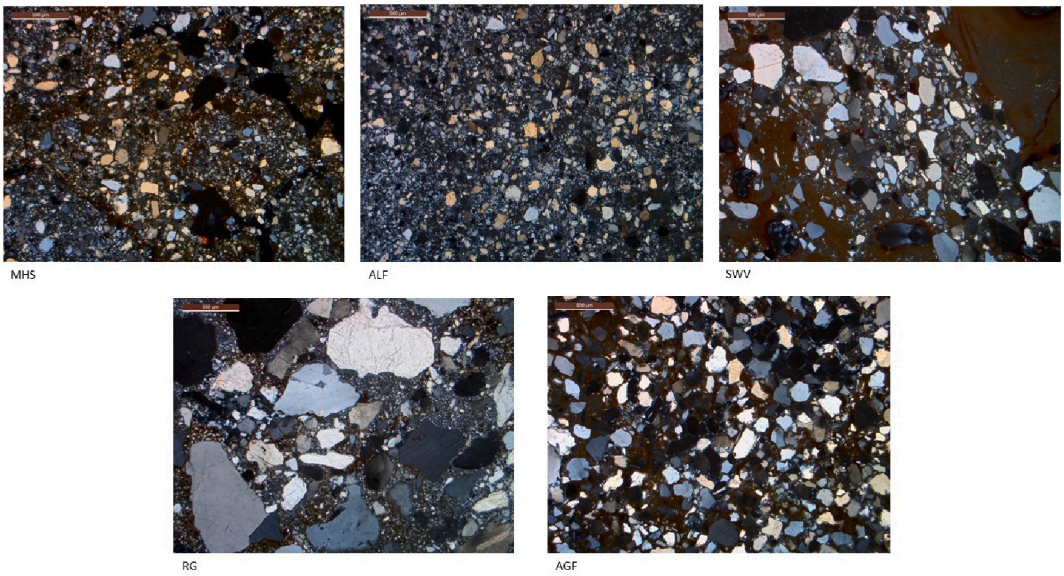

**Fig. 2.** Macro photos taken of fracture surfaces from the silcrete sources tested in the experiment. Polarized light. Scale bars are 500 μm. Photo credit: Kayley Elliott.

**Table 1**
Sample numbers and thicknesses.

| Sample | Thickness (μm) |
|---|---|
| MHS-1 | 704 |
| MHS-2 | 815 |
| ALF-1 | 838 |
| SWV-1 | 949 |
| SWV-2 | 721 |
| RG-1 | 882 |
| RG-2 | 1234 |
| AGF-1 | 748 |
| AGF-2 | 83 |

**Table 2**
Description of the texture (including clast/matrix ratio) of the silcrete sources tested in the experiment. Texture descriptions follow Summerfield (1983).

| Sample | Description |
|---|---|
| MHS | MHS is a pedogenic silcrete with conglomeratic texture (i.e. older generations of silcrete were re-cemented together). First- and second-generation silcretes have floating texture with rounded well-sorted quartz clasts of 50–100 μm. The cement of the second-generation silcrete is stained by impurities, consisting of poorly-sorted fine to coarse-grained microquartz crystals. |
| ALF | ALF is a pedogenic silcrete with floating texture. Poorly sorted clasts (mostly > 100 μm) are embedded in a relatively coarse-grained microquartz cement (cement cannot be distinguished from clasts everywhere). The cement in stained by impurities; clasts are rounded. |
| SWV | SWV1 is a pedogenic silcrete showing colluvial features (see Summerfield 1983). Sub-angular to slightly rounded quartz clasts (poorly sorted; 50–500 μm) are embedded in a strongly impurity-stained cement of fine microquartz. It has a floating texture. |
| RG | RG is a pedogenic silcrete with poorly sorted large quartz clasts (some measure up to 1 mm, some < 100 μm) sitting in a relatively fine microquartz cement that is stained by impurities. Clasts are angular but show dissolution bays. The silcrete has a floating texture. |
| AGF | AGF is a pedogenic silcrete with well-sorted angular clasts (up to 250 μm). It has a closely packed floating structure (for silcrete structure types see: Summerfield 1983); clasts are embedded in a strongly stained fine microquartz cement. |

Middle Stone Age artefacts made from material consistent with that source. SWV and AGF are the apparent major sources for the silcrete artefacts in the Doring River generally (Will et al., 2015; Shaw et al., 2019). Only the exploitation of RG is in question, though the nearby site Klein Kliphuis has >90% silcrete artefacts during certain periods (Mackay, 2011), and RG is the closest primary source identified so far.

The sources sampled reflect the few silcrete outcrops available in the Cederberg region of South Africa's West Coast, where silcrete is difficult to find. Sample numbers and thicknesses as determined by near infrared spectroscopy are summarized in Table 1. All samples were cut into plan-parallel slabs between 70 and 120 μm thick (diamond polished on both sides). Infrared transmission through these slabs was measured at normal incidence between 7000 and 2000 $cm^{-1}$ using Varian Cary 600 infrared spectrometer (Fig. 3).

### 2.1. Heating experiment

Heat-induced changes were recorded following protocols in Schmidt et al. (2011, 2017). The samples were dehydrated in a drying oven at 110 °C for 24 h. Spectra were recorded immediately after the samples had cooled to room temperature but before they reabsorbed atmospheric $H_2O$. The samples were then rehydrated in $H_2O$ at room temperature for 24 h to ensure pore spaces were completely filled, and a second spectrum was recorded. Samples were then heated to 200 °C for 4 h before the oven was set to cool to 110 °C (for a justification of the heating duration see (Schmidt, 2017)). Again, spectra were recorded before the samples reabsorbed atmospheric $H_2O$ and after rehydration for 24 h. This procedure was repeated at 50 °C increments up to a maximum temperature of 600 °C. All transmission measurements were recorded at room temperature.

### 2.2. Calculation of $H_2O$, SiOH, and pore volume

The molar absorption coefficients given by Scholze (1960) were used to calculate the concentration ($c$) of silanol and molecular water in the samples in wt% as:

$$c = \frac{MA}{10\rho_{SiO2}\alpha d}$$

with $M$ = molar mass of the water species: 18 g/mol for $H_2O$ and 17 g/mol for OH in silanol. $A$ = absorbance, $\rho_{SiO2}$ = density of quartz (2.65 g/$cm^3$), α = Scholze's absorption coefficient (1.14 L/mol cm for $H_2O$ and 160 L/mol cm $^2$ for silanol), and $d$ = sample thickness in cm.

The volume of intergranular open pore-space was calculated following protocols established by Schmidt *et al.* (2011, 2017) as follows:

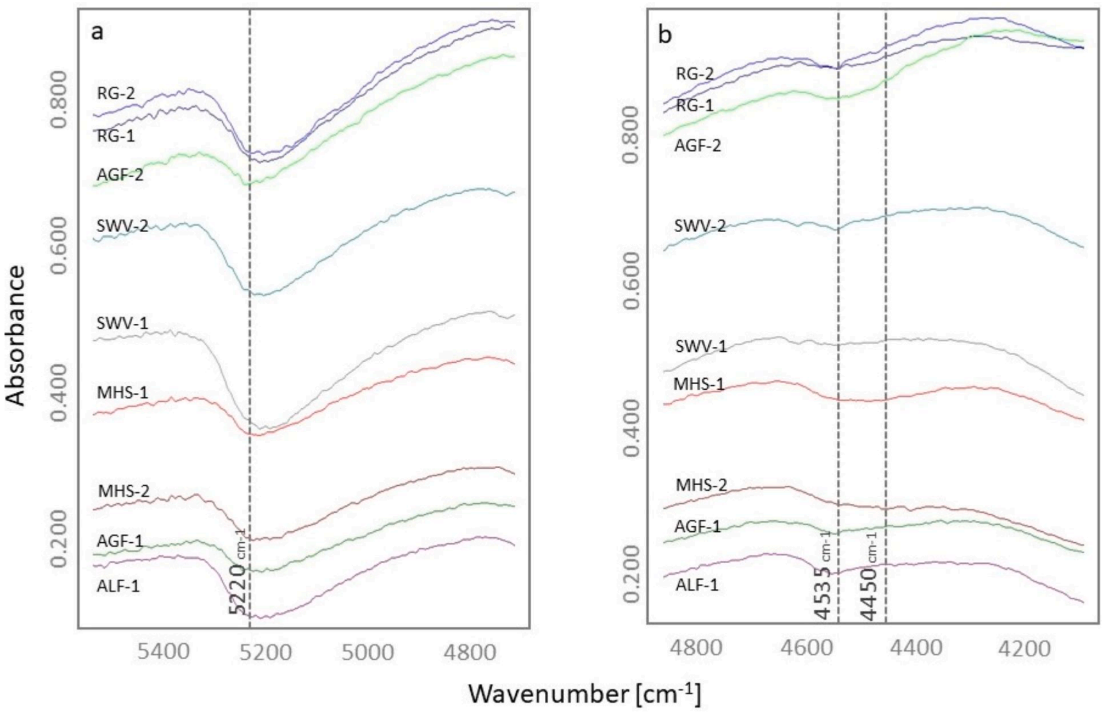

**Fig. 3.** NIR spectra recorded at room temperature. Starting concentrations of $H_2O$ **(a)** and SiOH **(b)** combination bands for all samples after baseline correction for readability. Note that all absorbances were measured on untreated spectra before baseline correction.

$H_2O$ content in the dehydrated sample is subtracted from $H_2O$ content in the rehydrated state of the same sample. The value produced corresponds to water that can be dehydrated, hence is held in the samples' open pores. This concentration in wt% was converted to open pore volume ($V_{(pores)}$, in vol%) by:

$$V_{(pores)} = cH_2O_{(pores)} / \left( \frac{(100 - c_{TiO2} - c_{H2O})}{\rho_{SiO2}} + \frac{c_{TiO2}}{\rho_{TiO2}} + c_{H2O} \right) \mathrm{x}100$$

with $cH_2O_{(pores)}$ = concentration of $H_2O$ held in open pores in wt%; $c_{TiO2}$ = concentration of anatase in wt% (we fixed this value to 0.5 wt% based on (Schmidt et al., 2017b)); $c_{H2O}$ = maximum concentration of $H_2O$ held in the sample in its hydrated state in wt%; $\rho_{SiO2}$ and $\rho_{TiO2}$ = the densities of quartz and anatase. Starting and ending concentrations of $H_2O$, SiOH, and pore space for each sample are summarized in Table 3.

### 2.3. Statistical analyses

Through their experiments, Mackay et al. (2018) showed that silcretes collected from different locations had different heating tolerances and fracture rates, so in addition to interpreting the data we also checked for similarities in thermal behavior between samples. Since silcrete is a heterogeneous material, we wanted to examine the degree of both within and between source variance in structural content and thermal behavior. We were also interested in examining whether materials from different sources responded differently to heat treatment under the same temperature conditions. This required fitting a model that describes flexible, curvilinear relationships between the structural variables of interest and temperature, while allowing for idiosyncratic effects of source and individual specimen. Therefore, the model has to allow for coefficients that are variable by source and likely also by individual specimen. Together these requirements suggest that a multilevel model incorporating a cubic spline basis (or other flexible nonlinear structure) is appropriate (see e.g. Brumback and Rice, 1998).

For an individual specimen *i*, from source *s*, at temperature *t*, the model for $H_2O$ (wt%) has the form

$$log_{10}\mathrm{H_2O}(i,s,t) = \beta_0 + Y_0(i) + Z_0(s) + \sum_{d=1}^{5} (\beta_d + Y_d(i) + Z_d(s))v_d(t) + \varepsilon(i,t),$$

where $\beta_0, \ldots \beta_5$ are the intercept and spline basis coefficients common to all observations (for a spline having five degrees of freedom, a reasonable degree of complexity for these data); $Y_0(i), \ldots Y_5(i)$ are unique

**Table 3**
Summary of starting and ending concentrations of $H_2O$, SiOH, pore volume ($m$ = mass as determined by the NIR absorption in the dehydrated state).

| Sample | Starting $m$ $H_2O$ (wt%) | Ending $m$ $H_2O$ (wt%) | Starting $m$ SiOH (wt%) | Ending $m$ SiOH (wt%) | Starting $m$ Pores (vol%) | Ending $m$ Pores (vol%) |
|---|---|---|---|---|---|---|
| MHS-1 | 0.46 | 0.09 | 0.35 | 0.05 | 0.31 | 0.38 |
| MHS-2 | 0.51 | 0.07 | 0.33 | 0.09 | 0.81 | 1.74 |
| ALF-1 | 0.61 | 0.22 | 0.63 | 0.11 | 2.77 | 1.57 |
| SWV-1 | 0.41 | 0.19 | 0.27 | 0.09 | 0.62 | 2.11 |
| SWV-2 | 0.25 | 0.04 | 0.20 | 0.05 | 0.19 | 0.66 |
| RG-1 | 0.27 | 0.15 | 0.10 | 0.05 | 0.61 | 1.05 |
| RG-2 | 0.28 | 0.17 | 0.09 | 0.04 | 0.89 | 1.32 |
| AGF-1 | 0.22 | 0.06 | 0.09 | 0.02 | 0.53 | 0.42 |
| AGF-2 | 0.24 | 0.09 | 0.13 | 0.04 | 0.43 | 0.65 |

contributions from individual *i*; $Z_0(s), \ldots Z_5(s)$ are unique contributions from source *s*; $v_d(t)$ is the $t^{th}$ element of the $d^{th}$ spline basis vector evaluated at temperature *t*; and $\varepsilon(i,t)$ is a Gaussian error term. We applied the $\log_{10}$ transform to $H_2O$ (wt%), as we did for SiOH (wt%) and pore volume (volume%), to stabilize its variance and enable the use of a Gaussian linear model. The models for SiOH and pore volume have forms analogous to the model above for $H_2O$. Because the model structure is the same for $H_2O$, SiOH and pore volume, and because these variables are pairwise correlated, we modeled the three variables jointly, therefore conducting a multivariate analysis of covariance.

We took a computational Bayesian approach to model-fitting because of the overall complexity of the model, as well as the need to learn fine details about components of variance described by $Y_0(i), \ldots Y_5(i)$ and $Z_0(s), \ldots Z_5(s)$ in the equation above (along with analogous components for SiOH and pore volume). We used a Hamiltonian Markov-chain Monte Carlo method to estimate model effects, as implemented in the *Stan* inference algorithms, accessed through the *brms* library of the statistical programming language *R* (Bürkner, 2017, 2018; R Core Team, 2017; Stan Development Team, 2020). We used independent Gaussian priors with mean zero and standard deviation 2 for the common coefficients $\beta_0, \ldots \beta_5$. Specimen-level contributions $Y_0(i), \ldots Y_5(i)$ were given a multivariate Gaussian prior with mean zero and variance–covariance matrix $\Sigma = D\,\Omega\,D$, where *D* is a diagonal matrix and $\Omega$ is a correlation matrix. The diagonal elements of *D* were given half-Cauchy priors with location zero and scale 1, and $\Omega$ was given an LKJ prior with parameter 1 (see, e.g., Stan User's Guide, "Multivariate Priors for Hierarchical Models") (Stan Development Team, 2020). Site-level contributions $Z_0(s), \ldots Z_5(s)$ were parameterized in the same way. Finally, each triad of residuals $\varepsilon_{H2O}(i, t)$, $\varepsilon_{SiOH}(i, t)$, $\varepsilon_{pore}(i, t)$ was given a multivariate Gaussian prior, with mean zero and a variance covariance matrix parameterized as above.

We allowed 3000 iterations as a warmup for each of four Markov-chain samplers, and then generated 1000 posterior samples per chain, resulting in a total of 4,000 parameter samples for inference. We checked diagnostics implemented in *brms* for adequacy of convergence. We investigated the goodness of fit of the model by examining a plot of the ordered Mahalanobis distances between observations and their predicted values, *versus* the quantiles of a chi-squared distribution on 3 degrees of freedom (Garrett, 1989).

## 3. Results

### 3.1. Changes in $H_2O$

Changes in $H_2O$ content for all samples are shown in Fig. 4. All samples show a decrease in $H_2O$ content from the lowest to highest temperatures, but differences in initial $H_2O$ concentration, the temperature at which changes begin, and magnitude of change are observable. Samples ALF-1 and MHS-2 had the highest starting $H_2O$ content [wt% 0.61 and 0.51, respectively]. Greatest average losses occurred in samples MHS-2 (≈45%), ALF-1 (≈39%), and MHS-1 (≈37%), while the smallest average losses occurred in samples RG-2 (≈11%) and RG-1 (≈12%). Most samples show an increase in $H_2O$ content after initial decrease occurring between 250°-300° C. Samples RG-1 and RG-2 decrease after this initial increase. $H_2O$ loss in samples from source MHS was linear, while all other sources showed an initial plateau in concentration. In these samples, loss begins after this plateau though the temperature at which this begins varies between 300°-400° C

### 3.2. Changes in SiOH

Fig. 5 shows change in SiOH content by temperature for each sample. Loss in SiOH content is observable for all samples. Starting concentration, thermal behavior, and magnitude of change are more highly variable than the corresponding $H_2O$ content. Sample ALF-1 had the highest starting SiOH content [wt% 0.63], at least 1.5 times greater than other samples. Greatest average losses occurred in samples ALF-1 (≈52%), and MHS-1 (≈30%), while the smallest average losses occurred in samples RG-1 and RG-2 (≈5%). Samples from sources RG, AGF, and SWV showed an initial increase in SiOH content occurring between 200°-250° C. Several samples also plateau in SiOH content between

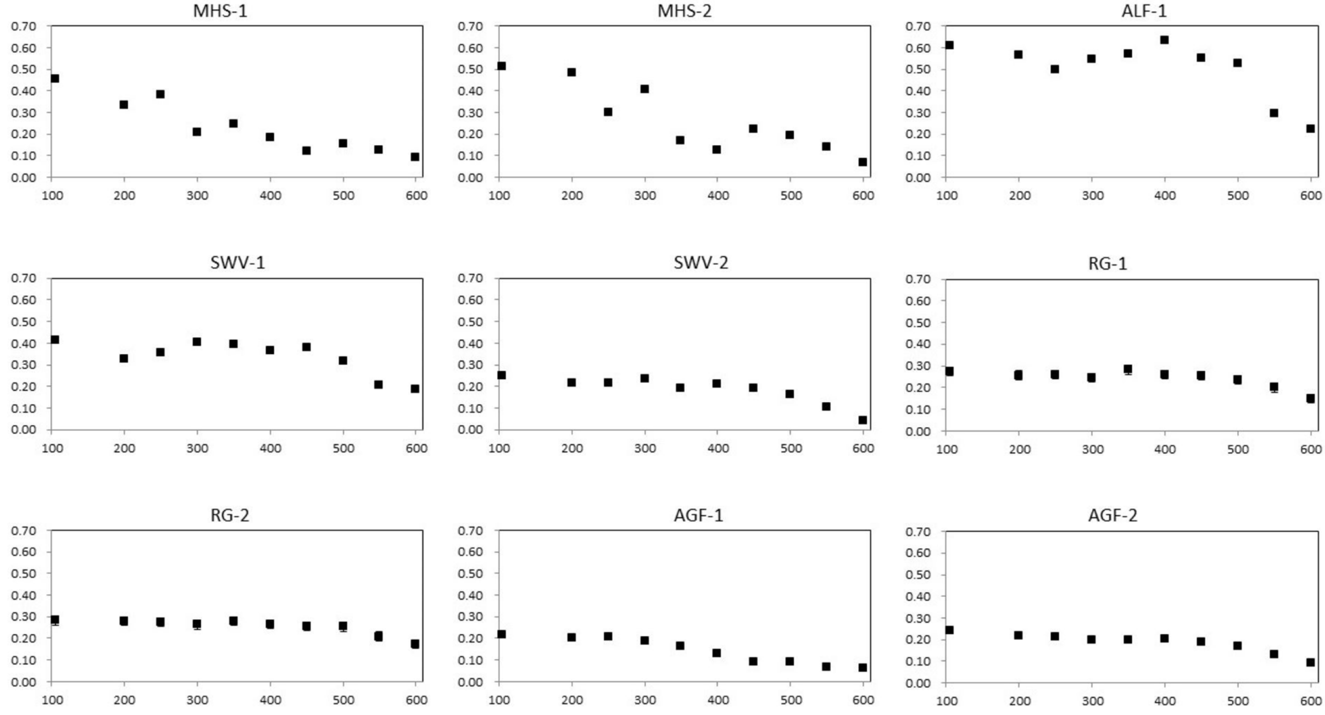

**Fig. 4.** Thermal evolution of structural $H_2O$ in silcrete samples. Concentrations are in wt%, calculated from the linear absorbance of the $H_2O$ combination band near 5200 $cm^{-1}$ in dehydrated samples, and plotted against heating temperature.

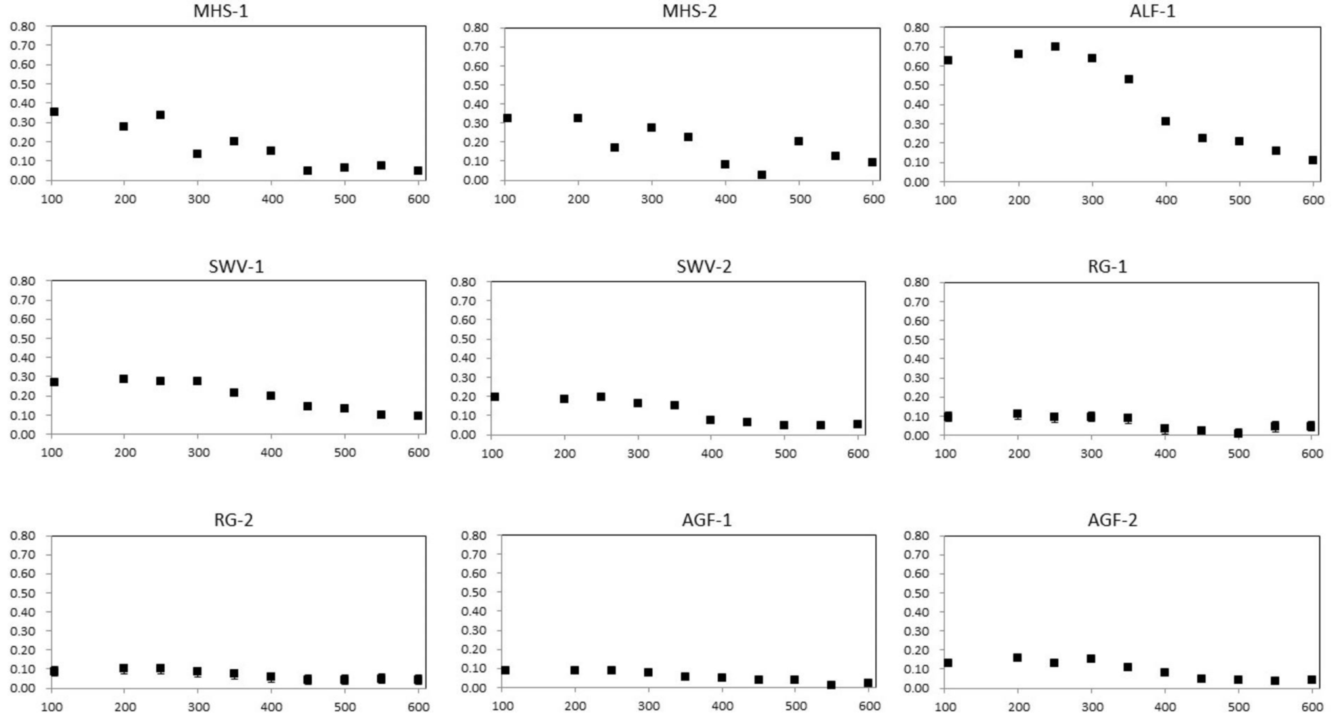

**Fig. 5.** Loss of SiOH in dehydrated silcrete samples. Concentrations are in wt%, calculated from the integral absorbance of the SiOH combination band near 4400 $cm^{-1}$, and plotted against heating temperature.

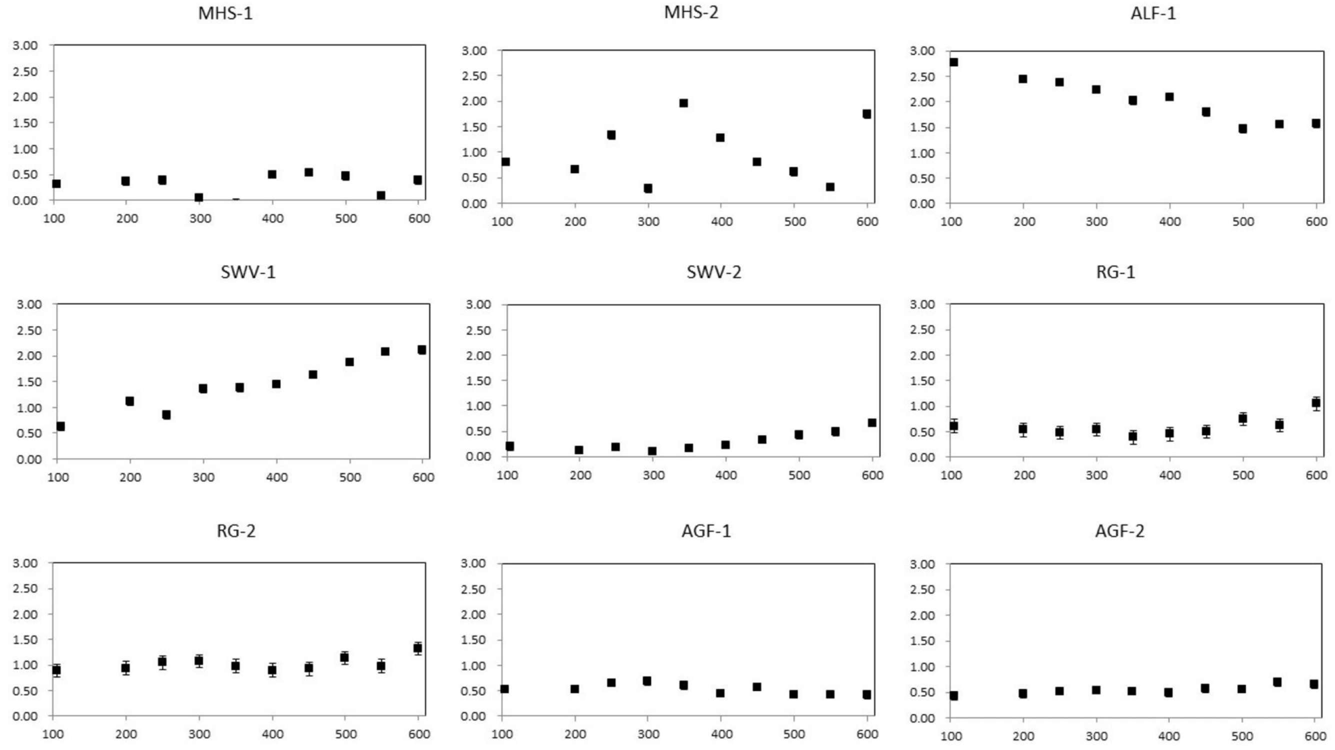

**Fig. 6.** Thermal evolution of intergranular pore space in silcrete samples. Pore space is in vol%, calculated from the mass of $H_2O$ loosely held in intergranular pores, and plotted against heating temperature.

450°-550° C, with the majority of thermal changes occurring before the plateau. Samples from source MHS behave differently, with both samples recording multiple increases and decreases in SiOH concentration during heating.

### 3.3. *Changes in pore space*

Changes in pore space showed the most variable response to heating (Fig. 6). Starting pore volume was greatest in sample ALF-1 [vol% 1.57], which contained three times or more of starting pore space than the

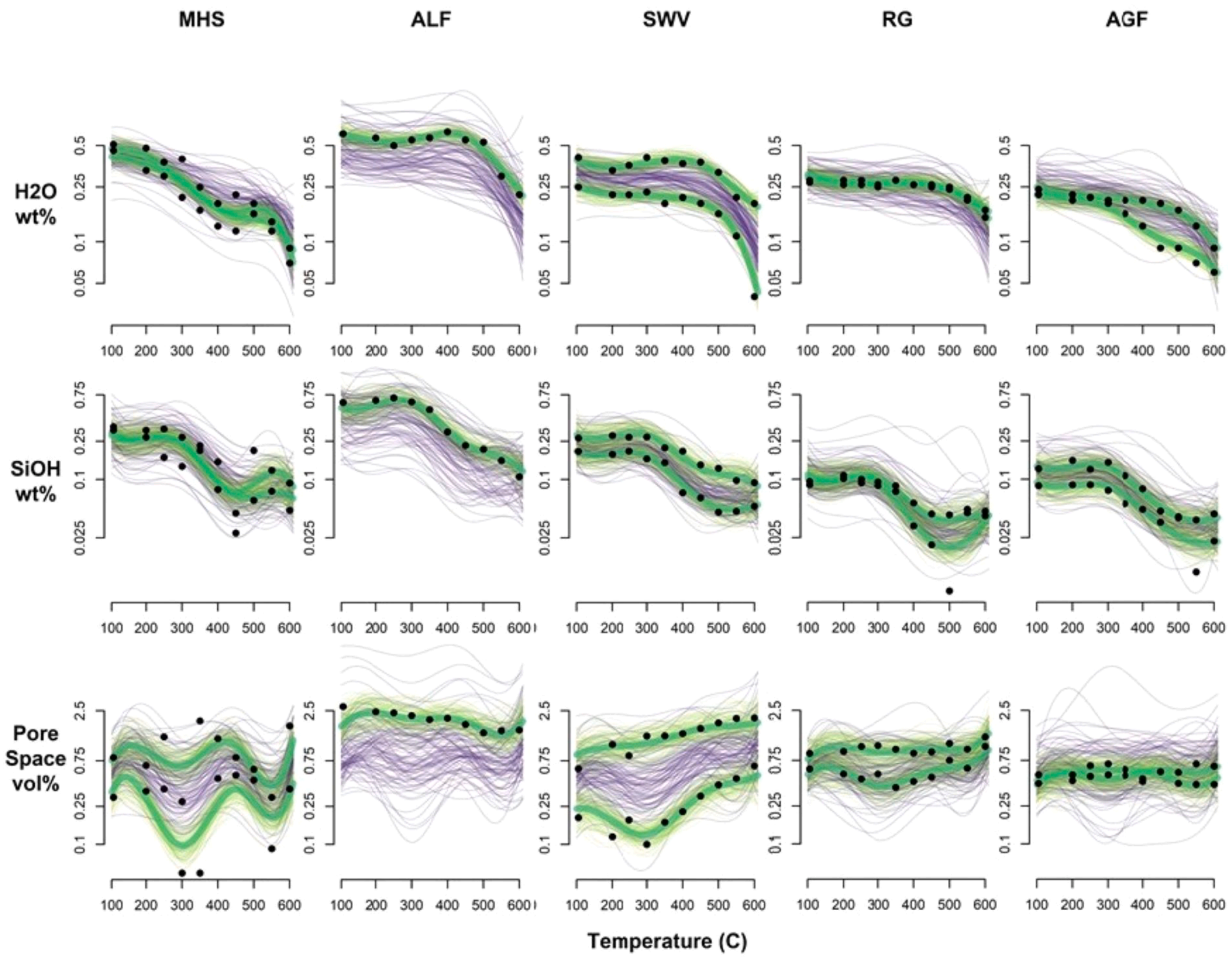

**Fig. 7.** Modeled curves for $H_2O$, SiOH, and pore space for all sources on the log 10 scale. The log 10 transformation was a necessary re-scaling for statistical modeling, though its effect in this graph is to visually compress percent-differences at the top of the vertical axis while stretching them at the bottom. Tick-marks along the vertical axes are labelled according to the original, untransformed scale. Thick green curves show model predictions for each specimen. Thin yellow and purple curves characterize model uncertainty for specimen- and source-level predictions, respectively. The latter curves were obtained from 100 random posterior samples from the fitted model. Specimen-level uncertainty is relatively small, hence the yellow curves are visually dominated by the green and purple curves. (For interpretation of the references to colour in this figure legend, the reader is referred to the web version of this article.)

other samples tested. Most samples gained pore space during heating at varying magnitudes. Most changes occurred after 300°-400° C. Greatest average gains occurred in samples SWV-1 (≈148%) and MHS-2 (≈93%), while the smallest average gains occurred in samples MHS-1 (≈7%) and AGF-2 (A ≈22%). Samples from source MHS record large drops and increases in pore volume that are not seen in samples from other sources. Instead of gaining additional pore volume, samples AGF-1 and ALF-1 lost pore space, with ALF-1 recording the greater average loss.

### 3.4. *Statistical analyses*

To understand the relative contributions of sources and individual samples to physio-chemical variation as temperature increases, we turn to the curvilinear statistical model. Modeled curves for $H_2O$, SiOH, and pore space for all samples after heating to different temperatures can be seen in Fig. 7. Fig. 7 displays smoothed specimen-level trends (thick green curves), along with specimen- and source-level uncertainty (thin yellow and purple curves, respectively). The relative contributions of specimens and sources to overall variation can be discerned visually by comparing the smoothed trends across specimens within sources, and subsequently across sources. Looking across the columns of Fig. 7 for a given physio-chemical parameter, we can see that source is the main component of variance for starting concentration and thermal behavior in $H_2O$, SiOH, and pore space, based on the fitted model. Although individual samples within sources vary in their responses to heating, sample-to-sample variation is dominated by source-level variation. Individual sample effects are most apparent in changes to pore space and in SiOH at higher temperatures. Specimens from source AGF are most consistent in thermal behavior, while pairs of specimens from other sources may perform very differently under heat treatment. The inclusion of only one specimen from ALF makes inferences about the thermal behavior of silcrete from this source difficult, in light of the high degree of site-level uncertainty indicated by the widths of the purple confidence envelopes for each of $H_2O$, SiOH, and pore space.

## 4. Discussion

### 4.1. *How much does structural composition change and what is the nature of change?*

Differences in starting concentrations and degree of change in $H_2O$, SiOH, and pore volume were present across sources. Samples from sources MHS and ALF recorded the greatest changes in $H_2O$ and SiOH concentration while concentrations in samples from source RG changed the least. Thermal changes in pore space followed a less consistent pattern of average change and more fluctuation during heating. An initial plateau is present in the samples before $H_2O$ and SiOH loss begin, representing the activation temperature required to begin breaking down H-O bonds. This is mirrored at higher temperatures, where plateaus represent the temperature after which few structural changes continue to occur. This supports the proposal by Schmidt *et.al.* (2017) of an ideal heating range for silcrete. The increase in SiOH in samples from sources RG, AGF, and SWV between 200°–250°C corresponds with the beginning of decreasing H-bond strength and the freeing of silanol from H-bonded water. The effect of this is an increasing specific absorption coefficient causing higher absorption values (Schmidt et al., 2011). The majority of $H_2O$ and SiOH loss is terminated by ~450 °C across samples, represented by another plateau in concentrations. In samples SWV-1 and ALF-1, a gain of structural water in closed pore space is observed. This indicates that $H_2O$ synthesized from SiOH is accumulated in fluid inclusions between 200 °C and 300–400 °C.

Our present study also yielded data on increases in pore space occurring with the concomitant formations of new siloxane bridges during the formation of new quartz crystal bonds. Both phenomena have been measured in heat-treated silcrete in past studies (Schmidt et al., 2017a, for example). Therefore, the question is not whether they take place, but rather how both can take place at the same time during heat treatment. New pore-space is most likely created by internal fracturing that happens as a consequence of relaxation of fluid inclusions at higher temperatures when high vapor pressure increases strain in the rocks. Si-O-Si may be formed at different locations in the rocks, still leading to changes in the rocks' overall fracture properties. Because the pore spaces in silcrete are rather variable in diameter, ranging from intergranular pores similar to the ones found in chert to macro-pores, these phenomena are not mutually exclusive in silcrete, and instead may take place at different locations within the rocks.

### 4.2. *What is the range of variation in silcrete behavior during heating?*

Most samples included in the experiment fell within the range of expectations based on published data for silcrete (Schmidt et al., 2011, 2017a; Schmidt et al., 2018; Schmidt, 2014). Data from Schmidt *et.al.* (2017) showed that silcrete samples tested increased in tightly held $H_2O$ between 300°-400 °C before decreasing around 450 °C, while most silanol was lost between 300°-450 °C. Most samples in our experiments show an increase in H2O content beginning around 250°-300 °C before loss occurs around 450 °C (Fig. 4), while silanol loss occurs primarily between 250°-450 °C (Fig. 5). However, the sample from source ALF differs from the other samples tested, losing more SiOH than $H_2O$ during heating and decreasing in porosity. The thermal behavior exhibited by the sample from source ALF is more similar to expectations from published data on chert, including its high starting concentrations of SiOH and the loss, rather than gain, of pore space (Schmidt et al., 2016; Schmidt et al., 2018). The trends shown indicate possible differences in internal fracture threshold for samples from different sources. Pore space increases as temperature increases for most samples, a trend that is typical of silcrete (Schmidt et al., 2017a). In contrast, the sample from source ALF decreased in pore space with increased temperature, a pattern more common to chert than silcrete (Schmidt et al., 2016; Schmidt et al., 2018). Samples from source MHS contained large voids and reservoirs between grains and do not seem to hold back $H_2O$ in open pores, which likely contributed to the signature of increasing and decreasing pore space.

Mackay et al. (2018) also tested samples from sources MHS (Mustard Hill) and ALF (referred to as 'Olifants River' in that paper) in their experiments. Samples from the two sources fractured at dramatically different rates when heated to high temperatures. All Mustard Hill samples remained intact across all temperature steps and volumes, while samples from the ALF/Olifants River source had the highest rate of exploded blocks of any silcrete source included in the experiments (Mackay et al., 2018). Fracturing during heat treatment is a function of vapor pressure from water that was not evacuated. Water not evacuated from a rock during heat treatment before surface pores close will also be heated, resulting in vapor pressure increase (Burnham et al., 1969; McLaren et al., 1983). Ramp rate is a function of how quickly free and molecularly bound water can be evacuated through open intergranular pores. Evacuation speed is not constant, but instead depends on sample size, $H_2O$/SiOH content, and pore volume (Schmidt, 2014; Schmidt et al., 2016; Schmidt et al., 2017a). Rocks with higher water content and lower porosity must be heated more slowly than more porous rocks with lower water content. Likewise, larger volumes of rock must be heated more slowly than smaller volumes (Schmidt, 2014).

Differences in the survivorship rates are likely a product of variation in water content and porosity between these silcretes. MHS samples showed some of the greatest losses in $H_2O$ and SiOH and increased in pore space during our experiments, which prevented buildup of enough vapor pressure to result in thermal fracture. Water evacuation was likely aided by the large voids noted for samples from this source. Decreasing pore volume with increased temperature observed from source ALF likely contributed to the high rates of fracture and explosion observed in the experiments by Mackay et al. (2018). The smallest samples from the ALF/Olifants River source survived heat treatment intact approximately 50% of the time while all samples of larger volumes fractured or exploded. As previously noted, pore space in the sample from source ALF decreased as temperature increased, a pattern more characteristic of chert than silcrete. This has implications for ramp rate and maximum temperature tolerance limits during heat treatment, suggesting that slower heating ramp rates are needed to prevent fracture from overheating.

### 4.3. *What is the primary component of variance influencing silcrete thermal behavior?*

Source was the primary component of variance of thermal behavior and magnitude of change across all documented variables. This supports the results of Mackay et al. (2018) indicating that source was the primary contributor to fracture rates within the silcrete sources examined. Individual sample effects on thermal behavior were also observed, though sample-to-sample variation within sources was dominated by variation across sources. Individual sample effects were most apparent in changes to pore volume and in SiOH at higher temperatures. This could indicate more variation in thermal behavior at higher temperatures or more predictable responses to heating at lower temperatures.

Determining source-level effects can be challenging. Fig. 7 describes modeled specimen and source effects and characterizes uncertainty for specimen- and source-level predictions. When considering source ALF, where $n = 1$, panels are dominated by purple curves. This reflects the difficulty in characterizing source effects for a single sample. However, uncertainty is not high for most sources and therefore source-specific signatures of thermal behavior can be discerned. Because our model is made to be sensitive to sources of variation, a clear and well-supported source effect will be captured, even with a small sample. For example, modeled SiOH trajectories are different for each source. Source-level effects were harder to capture for MH and ALF, as seen by the wide spread of thin purple curves, but are very clear for SWV, RG, and AGF, where purple curves are more constrained and generally fall close to the specimen effects.

## 5. Conclusions

The structural composition of silica rocks affects their heating tolerances and thermal-induced changes to mechanical properties. Results from Mackay et al. (2018) suggest a possible relationship between the structural changes that occur within silcretes and their rate of failure from overheating when heat-treated quickly to high temperatures.

Differences in starting concentrations of $H_2O$, SiOH, and pore volume and the rate of structural change within silcrete samples may also affect the degree of change to fracture toughness, which in turn may result in variation in the flaked products produced from a particular source. Future research should include expanding NIR data sets to encompass samples from other areas of southern Africa to better understand the degree of variation in structural content present, as well as trends in the thermal behavior of silcretes. Controlled heating experiments are needed to evaluate whether heating parameters affect the rate and nature of structural change, as well as explore possible relationships between structural content and heat-induced fracture. Finally, experiments should be conducted to observe how source and heating temperature affect mechanical properties, flake formation, flake dimensions, and attributes.

## Declaration of Competing Interest

The authors declare that they have no known competing financial interests or personal relationships that could have appeared to influence the work reported in this paper.

## Acknowledgements

SW was supported by a National Science Foundation (NSF) Graduate Research Fellowship (fellow ID 2017251536) and NSF research grant (award number 1324719). SN was supported by a University of Wollongong Future Fellow Scholarship and School of Medicine and Health Science Travel Grant. Financial support for AM was provided by the Centre for Archaeological Science and the University of Wollongong. Financial support of PS was provided by the Deutsche Forschungsgemeinschaft (DFG) (grant number SCHM 3275/2-1). We also thank C.E. Miller for providing access to the IR spectrometer. Thank you to Kayley Elliott for providing the images as part of a Summer Internship Program funded by the University of Wollongong Centre for Archaeological Science.

## References

Backwell, L., d'Errico, F., Wadley, L., 2008. Middle Stone Age bone tools from the Howiesons Poort layers, Sibudu Cave, South Africa. J. Archaeol. Sci. 35 (6), 1566–1580.

Bleed, P., Meier, M., 1980. An Objective Test of the Effects of Heat Treatment of Flakeable Stone. Am. Antiq. 45 (3), 502–507.

Brown, K.S., Marean, C.W., Herries, A.I.R., Jacobs, Z., Tribolo, C., Braun, D., Roberts, D. L., Meyer, M.C., Bernatchez, J., 2009. Fire As an Engineering Tool of Early Modern Humans. Science 325 (5942), 859–862.

Brumback, B.A., Rice, J.A., 1998. Smoothing spline models for the analysis of nested and crossed samples of curves. J. Am. Stat. Assoc. 93 (443), 961–976.

Bürkner, P., 2017. brms: An R Package for Bayesian Multilevel Models Using Stan. J. Stat. Softw. 80, 1–28.

Bürkner, P., 2018. Advanced Bayesian Multilevel Modeling with the R Package brms. The R Journal. 10, 395–411.

Burnham, C.W., Holloway, J.R., Davis, N.F., 1969. Thermodynamic properties of water to 1, 0000 C and 10,000 bars. Geological Society of America.

Domanski, M., Webb, J.A., Boland, J., 1994. Mechanical Properties of Stone Artefact Materials and the Effect of Heat Treatment*. Archaeometry. 36 (2), 177–208.

Flrke, O.W., Khler-Herbertz, B., Langer, K., Tnges, I., 1982. Water in microcrystalline quartz of volcanic origin: Agates. Contrib. Miner. Petrol. 80 (4), 324–333.

Fukuda, J., Peach, C.J., Spiers, C.J., Nakashima, S., 2009. Electrical impedance measurement of hydrous microcrystalline quartz. J. Mineral. Petrol. Sci. 104 (3), 176–181.

Garrett, R.G., 1989. The chi-square plot: a tool for multivariate outlier recognition. J. Geochem. Explor. 32 (1-3), 319–341.

Graetsch, H., Flrke, O.W., Miehe, G., 1985. The nature of water in chalcedony and opal-C from brazilian agate geodes. Phys. Chem. Miner. 12 (5), 300–306.

Graetsch, H., Flrke, O.W., Miehe, G., 1987. Structural defects in microcrystalline silica. Phys. Chem. Miner. 14 (3), 249–257.

Henshilwood, C.S., D'errico, F., Marean, C.W., Milo, R.G., Yates, R., 2001. An early bone tool industry from the Middle Stone Age at Blombos Cave, South Africa: implications for the origins of modern human behaviour, symbolism and language. J. Hum. Evol. 41 (6), 631–678.

Kronenberg, A.K., 1994. Hydrogen speciation and chemical weakening of quartz. In: Silica: Physical Behaviour, Geochemistry and Materials Applications, Reviews in Mineralogy 29. Mineralogical Society of America, Washington, pp. 123–176.

Lombard, M., Wadley, L., 2016. Hunting Technologies During the Howiesons Poort at Sibudu Cave: What They Reveal About Human Cognition in KwaZulu-Natal, South Africa, Between ~65 and 62 ka. In: Multidisciplinary Approaches to the Study of Stone Age Weaponry, Vertebrate Paleobiology and Paleoanthropology. Springer, Dordrecht, pp. 273–286.

Mackay, A., 2011. Nature and significance of the Howiesons Poort to post-Howiesons Poort transition at Klein Kliphuis rockshelter, South Africa. J. Archaeol. Sci. 38 (7), 1430–1440.

Mackay, A., Lin, S.C., Kenna, L.S., Blackwood, A.F., 2018. Variance in the response of silcrete to rapid heating complicates assumptions about past heat treatment methods. Archaeological and Anthropological Sciences.

McLaren, A.C., Cook, R.F., Hyde, S.T., Tobin, R.C., 1983. The mechanisms of the formation and growth of water bubbles and associated dislocation loops in synthetic quartz. Phys. Chem. Miner. 9 (2), 79–94.

Micheelsen, H., 1966. The Structure of Dark Flint from Stevns, Denmark (PhD thesis). University of Copenhagen, Odense.

Mourre, V., Villa, P., Henshilwood, C.S., 2010. Early Use of Pressure Flaking on Lithic Artifacts at Blombos Cave, South Africa. Science 330 (6004), 659–662.

Pargeter, J., 2007. Howiesons Poort Segments as Hunting Weapons: Experiments with Replicated Projectiles. The South African Archaeological Bulletin. 62, 147–153.

Pargeter, J., Schmidt, P., 2020. 'Simple' surface-fire heat treatment significantly improves silcrete flake quality and flaking efficiency. J. Archaeolog. Sci.: Rep. 30, 102203. https://doi.org/10.1016/j.jasrep.2020.102203.

R Core Team, 2017. R: A language and environment for statistical computing. R Foundation for Statistical Computing, Vienna, Austria.

Roqué-Rosell, J., Torchy, L., Roucau, C., Lea, V., Colomban, P., Regert, M., Binder, D., Pelegrin, J., Sciau, P., 2011. Influence of Heat Treatment on the Physical Transformations of Flint Used by Neolithic Societies in the Western Mediterranean | MRS Online Proceedings Library (OPL) | Cambridge Core. MRS Online Proceedings Library Archive. 1319.

Schindler, D.L., Hatch, J.W., Hay, C.A., Bradt, R.C., 1982. Aboriginal Thermal Alteration of a Central Pennsylvania Jasper: Analytical and Behavioral Implications. Am. Antiq. 47 (3), 526–544.

Schmidt, P., 2014. What causes failure (overheating) during lithic heat treatment? Archaeological Anthropological Sci. 6 (2), 107–112.

Schmidt, P., 2017. How reliable is the visual identification of heat treatment on silcrete? A quantitative verification with a new method. Archaeological Anthropological Sci. 11 (2), 713–726.

Schmidt, P., Badou, A., Fröhlich, F., 2011. Detailed FT near-infrared study of the behaviour of water and hydroxyl in sedimentary length-fast chalcedony, SiO2, upon heat treatment. Spectrochim. Acta Part A Mol. Biomol. Spectrosc. 81 (1), 552–559.

Schmidt, P., Buck, G., Berthold, C., Lauer, C., Nickel, K.G., 2018. The mechanical properties of heat-treated rocks: a comparison between chert and silcrete. Archaeological and Anthropological Sciences.

Schmidt, P., Lauer, C., Buck, G., Miller, C.E., Nickel, K.G., 2017a. Detailed near-infrared study of the 'water'-related transformations in silcrete upon heat treatment. Phys. Chem. Miner. 44 (1), 21–31.

Schmidt, P., Masse, S., Laurent, G., Slodczyk, A., Le Bourhis, E., Perrenoud, C., Livage, J., Fröhlich, F., 2012. Crystallographic and structural transformations of sedimentary chalcedony in flint upon heat treatment. J. Archaeol. Sci. 39 (1), 135–144.

Schmidt, P., Nash, D.J., Coulson, S., Göden, M.B., Awcock, G.J., 2017b. Heat treatment as a universal technical solution for silcrete use? A comparison between silcrete from the Western Cape (South Africa) and the Kalahari (Botswana). PLOS ONE. 12, e0181586.

Schmidt, P., Paris, C., Bellot-Gurlet, L., 2016. The investment in time needed for heat treatment of flint and chert. Archaeological Anthropological Sci. 8 (4), 839–848.

Schmidt, P., Stynder, D., Conard, N.J., Parkington, J.E., 2020. When was silcrete heat treatment invented in South Africa? Palgrave 6 (1). https://doi.org/10.1057/s41599-020-0454-z.

Scholze, H., 1960. Über die quantitative UR-spektroskopische Wasser- bestimmung in Silikaten. Fortschr Mineral. 38, 122–123.

Shaw, M., Ames, C., Phillips, N., Chambers, S., Dosseto, A., Douglass, M., Goble, R., Jacobs, Z., Jones, B., Lin, S., Low, M., McNeil, J.-L., Nasoordeen, S., O'Driscoll, C., Saktura, R., Sumner, A., Watson, S., Will, M., Mackay, A., 2019. The Doring River Archaeology Project: Approaching the evolution of human land use patterns in the Western Cape. South Africa. PalaeoAnthropology. 400, 422.

Stan Development Team, 2020. RStan: the R interface to Stan.

Steele, T.E., Mackay, A., Fitzsimmons, K., Igreja, B., Marwick, B., Orton, J., Schwortz, S., Stahlschmidt, M., 2016. Varsche Rivier 003: A Middle and Later Stone Age site with Still Bay and Howiesons Poort assemblages in southern Namaqualand, South Africa. PaleoAnthropology. 2016, 100–163.

Summerfield, M.A., 1983. Geochemistry of weathering profile silcretes, southern Cape Province, South Africa. Geological Society, London, Special Publications. 11 (1), 167–178.

Tucker, M.E., 2009. Sedimentary Petrology: An Introduction to the Origin of Sedimentary Rocks. John Wiley & Sons.

Wadley, L., 2010. Compound-Adhesive Manufacture as a Behavioral Proxy for Complex Cognition in the Middle Stone Age. Current Anthropology. 51 (S1), S111–S119.

Will, M., Mackay, A., Phillips, N., 2015. Implications of Nubian-Like Core Reduction Systems in Southern Africa for the Identification of Early Modern Human Dispersals. PLOS ONE. 10, e0131824.